

GRAVITY-MODES IN ZZ CETI STARS

III. EIGENVALUES AND EIGENFUNCTIONS

Yanqin Wu^{1,2} and Peter Goldreich¹

ABSTRACT

We report on numerical calculations of nonadiabatic eigenvalues and eigenfunctions for g-modes in ZZ Ceti variables. The spectrum of overstable $\ell = 1$ modes delineates the instability strip. Its blue edge occurs where $\omega\tau_c \approx 1$ for the $n = 1$ mode. Here ω is radian frequency and τ_c is about four times the thermal timescale at the bottom of the surface convection zone. As a ZZ Ceti cools, its convection zone deepens, longer period modes become overstable, but the critical value of $\omega\tau_c$ separating overstable and damped modes rises. The latter is a consequence of enhanced radiative damping for modes which propagate immediately below the convection zone. The critical value of $\omega\tau_c$ is of observational significance because modes with the smallest value of $\omega\tau_c$ are most observable photometrically. Maximum periods for overstable modes predicted for our cooler model envelopes are about a factor two longer than the observational upper limit of 1,200 s. We assess a number of plausible resolutions for this discrepancy among which convective overshoot and nonlinear saturation look promising. The nonadiabatic eigenfunctions enable us to predict relative amplitudes and phases of photospheric variations of flux and velocity, quantities made accessible by recent observations. We also present asymptotic formula for damping rates of high order modes, a result of consequence for future investigations of nonlinear saturation of the amplitudes of overstable modes.

1. Introduction

While passing through a narrow temperature range around $T_{\text{eff}} \sim 12,000$ K, DA (hydrogen) white dwarfs exhibit pulsations with periods between 2 and 20 minutes. These oscillations are identified with g-modes having radial orders $1 \leq n \leq 30$, and spherical harmonic degrees $1 \leq \ell \leq 2$. Mode overstability occurs when driving in the thin and fast reacting surface convection zone exceeds damping in the underlying radiative interior (Brickhill 1991, Gautschy et al. 1996, Goldreich & Wu 1998, hereafter Paper I). The flux perturbation entering the convection zone from the underlying radiative interior is in phase with the pressure perturbation. Because the convection is fast and efficient, the specific entropy perturbation is nearly depth-independent throughout the bulk of the convection zone. Consequently, the magnitude of the flux perturbation decreases outward. The phase relation between the pressure and flux perturbations then results in convective driving.

Gravity-modes have simple structures in their upper evanescent regions. This permits an analytic derivation of a stability criterion based on the quasiadiabatic approximation for modes whose evanescent regions extend well below the base of the convection ‘zone. Overstability is predicted provided $\omega\tau_c > 1$, where τ_c is a few times the thermal time scale at the bottom of the convection zone. Applied blindly, this

¹Theoretical Astrophysics, California Institute of Technology 130-33, Pasadena, CA 91125, USA; pmg@gps.caltech.edu

²Astronomy Unit, School of Mathematical Sciences, Queen Mary and Westfield College, Mile End Road, London E1 4NS, UK; Y.Wu@qmw.ac.uk

criterion predicts overstability in cool ZZ Ceti for modes whose periods far exceed those observed. Our numerical calculations enable us to drop both the quasiadiabatic approximation and the restriction that the evanescent region extend well below the convection zone. They also allow us to incorporate the effect of turbulent viscosity as discussed in Brickhill (1990) and Goldreich & Wu (1998, hereafter Paper II).

This paper is the third in a series dedicated to the overstability of gravity-modes in ZZ Ceti. It is largely numerical, and presents results of nonadiabatic calculations of eigenvalues and eigenfunctions. Nonadiabaticity is important for modes which have $\omega\tau_c \lesssim 1$, since they have $\tau_{\text{th}} < 1$ in their driving and damping regions. This category includes both overstable modes with $\omega\tau_c \approx 1$, which are easily detectable by photometric measurements, and damped modes with $\omega\tau_c \ll 1$, whose excitation by parametric instability acts to limit the amplitudes of overstable modes. It is imperative that our calculations accurately represent them.

The organization of this paper is as follows. In §2, we collect the equations which govern linear, nonadiabatic oscillations, establish appropriate boundary conditions, and describe the method we use to construct envelope models for ZZ Ceti. In §3 we assess the magnitude of nonadiabatic effects in the evanescent and propagating regions of g-modes. Numerical techniques employed to solve the eigenvalue problem are elaborated in §4. The impact of nonadiabaticity and turbulent viscosity on g-mode eigenvalues and eigenfunctions is described in §5. We then discuss in §6 several possibilities to reconcile the nonadiabatically calculated spectra of overstable modes with those observed. A short summary follows in §7. The appendix is devoted to analysis of a toy model which elucidates the asymptotic damping rates of high order modes.

Symbols used in this paper are defined in Table 1. Their usage is consistent with that in previous papers of this series.

[t]

2. Equations and Boundary Conditions

2.1. Equations in the Radiative Region

The linearized equations describing nonadiabatic pulsations read

$$\frac{\delta\rho}{\rho} = -ik_h\xi_h - \frac{d\xi_z}{dz}, \quad (1)$$

$$\frac{\omega^2}{g}\xi_h = ik_h\left(\frac{p}{g\rho}\frac{\delta p}{p} - \xi_z\right), \quad (2)$$

$$\frac{\omega^2}{g}\xi_z = \frac{p}{\rho g}\frac{d}{dz}\left(\frac{\delta p}{p}\right) - \frac{d\xi_z}{dz} + \frac{\delta p}{p} - \frac{\delta\rho}{\rho}, \quad (3)$$

$$\delta s = \frac{iFm_p}{\omega\rho k_B T}\frac{d}{dz}\left(\frac{\delta F}{F}\right), \quad (4)$$

$$\frac{\delta F}{F} = (4 - \kappa_T)\frac{\delta T}{T} - (1 + \kappa_\rho)\frac{\delta\rho}{\rho} - \frac{d\xi_z}{dz} + \frac{p}{\rho g\nabla}\frac{d}{dz}\left(\frac{\delta T}{T}\right), \quad (5)$$

for plane-parallel geometry with the Cowling approximation, and an assumed time-dependence of $\exp^{-i\omega t}$. Equations (1)-(4) express the conservation of mass, horizontal and vertical momentum, as well as energy. Equation (5) describes the equation of radiative diffusion. Closure of this system of equations requires

Table 1. DEFINITIONS

Symbol	Meaning
R	stellar radius
g	surface gravity
z	depth below photosphere
z_b	depth at bottom of convection zone
z_ω	depth at top of mode's cavity, $z_\omega \sim \omega^2/(gk_h^2)$
ω	radian mode frequency, $\omega = \omega_r + i\omega_i$
n	radial order of mode
ℓ	angular degree of mode
k_h	horizontal wave vector, $k_h^2 = \ell(\ell + 1)/R^2$
k_z	vertical wave vector
ρ	mass density, ρ_b mass density at $z = z_b$
p	pressure
T	temperature
s	specific entropy in units of k_B/m_p
F	energy flux
c_s	adiabatic sound speed, $c_s^2 = (\partial p/\partial \rho)_s = \Gamma_1 p/\rho$
ρ_s	$\rho_s \equiv (\partial \ln \rho/\partial s)_p$
δ	denotes Lagrangian perturbation
ξ_h	horizontal component of displacement vector
ξ_z	vertical component of displacement vector
v_h	horizontal component of velocity vector
f	coefficient measuring convective inefficiency
v_{cv}	convective velocity, $v_{cv} \sim (F/\rho)^{1/3}$
t_{cv}	response time for convection, $t_{cv} \sim z/v_{cv}$
A, B, C	dimensionless constants approximately 2, 8 & 8 for ZZ Cetus
τ_{th}	thermal constant at depth z , $t_{cv}/\tau_{th} \sim (v_{cv}/c_s)^2$ in the convection zone
τ_ω	thermal time at $z = z_\omega$
τ_b	unconventional thermal time constant at z_b , $\tau_b \approx \tau_{th}/5$ at z_b .
τ_c	time constant of low pass filter for convection zone, $\tau_c = (B + C)\tau_b$
N^2	Brunt-Väisälä frequency
κ_T, κ_ρ	opacity derivatives, $\kappa_T \equiv (\partial \ln \kappa/\partial \ln T)_\rho$, $\kappa_\rho \equiv (\partial \ln \kappa/\partial \ln \rho)_T$
c_p	dimensionless heat capacity, $c_p \equiv (\partial s/\partial \ln T)_p$
∇	temperature gradient, $\nabla \equiv d \ln T/d \ln p$
∇_{ad}	adiabatic temperature gradient, $\nabla_{ad} \equiv (\partial \ln T/\partial \ln p)_s$

constitutive relations for the equation of state and the opacity. Setting $\delta s = 0$ reduces the above equations to the adiabatic ones studied in Paper I.

We choose δp and δs as our independent thermodynamic variables and set

$$\frac{\delta \rho}{\rho} = \frac{1}{\Gamma_1} \frac{\delta p}{p} + \rho_s \delta s, \quad (6)$$

$$\frac{\delta T}{T} = \nabla_{ad} \frac{\delta p}{p} + \frac{\delta s}{c_p}. \quad (7)$$

Then the linear perturbation equations may be written as four first-order differential equations for the four dependent variables $\delta p/p$, $d(\delta p/p)/d \ln p$, $\delta F/F$, and δs ;

$$\frac{d}{d \ln p} \left(\frac{\delta p}{p} \right) = X, \quad (8)$$

$$\frac{dX}{d \ln p} = - \left(\frac{p}{g\rho} \right)^2 \left[k_h^2 \left(\frac{N^2}{\omega^2} - 1 \right) + \left(\frac{\omega}{c_s} \right)^2 \right] \left(\frac{\delta p}{p} \right) - X + \left(\frac{p}{g\rho} \right) \frac{(gk_h)^2 - \omega^4}{g\omega^2} \rho_s \delta s, \quad (9)$$

$$\frac{d}{d \ln p} \left(\frac{\delta F}{F} \right) = \frac{-i\omega k_B T p}{g m_p F} \delta s, \quad (10)$$

$$\begin{aligned} \frac{1}{c_p \nabla} \frac{d\delta s}{d \ln p} = & - \left[(4 - \kappa_T) \nabla_{ad} - \frac{\kappa_\rho}{\Gamma_1} - \left(1 - \frac{\omega^2 p}{g^2 \rho} \right) \frac{(gk_h)^2}{(gk_h)^2 - \omega^4} + \frac{1}{\nabla} \frac{d\nabla_{ad}}{d \ln p} \right] \left(\frac{\delta p}{p} \right) \\ & - \left[\frac{\nabla_{ad}}{\nabla} - \frac{(gk_h)^2}{(gk_h)^2 - \omega^4} \right] X + \left(\frac{\delta F}{F} \right) - \left[\frac{(4 - \kappa_T)}{c_p} - \kappa_\rho \rho_s + \frac{1}{\nabla} \frac{d}{d \ln p} \left(\frac{1}{c_p} \right) \right] \delta s. \end{aligned} \quad (11)$$

The perturbation equations are to be solved as an eigenvalue problem. Since equation (10) includes a factor i , all four dependent variables and the eigenfrequency are *complex*. We write each complex variable in the form

$$Q = (Q_r + iQ_i) \exp^{-i\omega t}. \quad (12)$$

The physical perturbation is given by $\text{Re}(Q) = e^{\omega_i t} (Q_r \cos \omega_r t + Q_i \sin \omega_r t)$.

2.2. Equations in the Convection Zone

Inside the convection zone, g-mode perturbations are constrained by the rapid response of convection to the instantaneous pulsational state (Brickhill 1990 & 1991, Papers I & II). Rapid momentum diffusion enforces

$$|X| = \left| \frac{d}{d \ln p} \left(\frac{\delta p}{p} \right) \right| \ll \frac{z}{z_\omega} \left| \frac{\delta p}{p} \right|. \quad (13)$$

And fast entropy mixing ensures that

$$\left| \frac{d\delta s}{d \ln p} \right| \ll \frac{z}{z_\omega} |\delta s|, \quad (14)$$

except in the thin superadiabatic layer. The entropy gradient in the superadiabatic layer is non-negligible and increases with increasing convective flux. But as this region is thin and has low mass, it is sufficient to incorporate its effect into the boundary conditions. The total, convective plus radiative, flux perturbation follows from equation (10). whereas equation (11) determines the radiative flux perturbation in terms of δp and δs .

2.3. Boundary Conditions

Solving four linear, homogeneous, first-order, ordinary differential equations to obtain eigenvalues and eigenfunctions, requires a total of five boundary conditions. Four of these express physical constraints imposed by the environment outside the domain in which the differential equations are to be integrated. The fifth merely sets the magnitude scale and phase for the eigenfunctions.

Approximations described in §2.2 enable us to lower the outer boundary from the photosphere to the top of the radiative interior at z_b . The three boundary conditions applied there read:

$$\left(\frac{\delta p}{p}\right) = C, \tag{15}$$

$$X = \frac{-k_h^2}{\omega^2 p_b} \int_0^{p_b} dp \frac{p \rho_s}{\rho} \left[\frac{ds}{d \ln p} \left(\frac{\delta p}{p}\right) - \delta s \right], \tag{16}$$

$$\delta s = \frac{(B + C)}{1 - i\omega\tau_c} \left(\frac{\delta F}{F}\right). \tag{17}$$

The constant C in equation (15) sets the scale and phase of the eigenfunction. Equation (16) follows from the near vanishing of X in the convection zone, as expressed by equation (13), together with equations (20) and (21) of Paper II, which account for the jump in X across the convective-radiative boundary. Equation (17) relates the entropy perturbation in the main part of the convection zone to the flux perturbation that enters from below (see Paper I).

It is advantageous to raise the bottom boundary from the center of the star to a depth, $z = z_{\text{deep}}$, where the quasiadiabatic approximation is valid and the plane-parallel approximation still applies. This step alters the spectrum of eigenvalues ω . However, a simple procedure to be described later allows us to recover values for ω_i appropriate to a complete stellar model. We generally take $z = z_{\text{deep}}$ to be the level at which $p = 10^{16}$ dyne cm⁻². Since $\tau_{\text{th}} \approx 10^{10}$ s at z_{deep} , the quasiadiabatic approximation is valid there for all g-modes of interest to our investigation. And in DA white dwarf models provided to us by Bradley (1996), the region above z_{deep} extends over the outer 2 percent of the stellar radius and includes about 10^{-6} of the stellar mass. The two boundary conditions imposed at $z = z_{\text{deep}}$ are

$$X + \left(1 - \frac{k_h^2 p}{\omega^2 \rho}\right) \frac{\delta p}{p} = 0, \tag{18}$$

$$\left(\frac{\delta F}{F}\right) + M_1 \left(\frac{\delta p}{p}\right) + M_2 X = 0. \tag{19}$$

The mechanical boundary condition given by equation (18) states that $\xi_z = 0$ at $z = z_{\text{deep}}$. It follows from equations (2) and (3). Thus our model is bounded from below by a rigid wall. Equation (19) is our thermal boundary condition. It is the quasiadiabatic limit of the radiative diffusion equation (11) which defines the coefficients M_1 and M_2 . Our lower boundary conditions are somewhat arbitrary. For example, we could have adopted $d\xi_h/dz = 0$ and $\delta s = 0$ as mechanical and thermal boundary conditions. However, because δs decreases rapidly with depth, taking $\delta s = 0$ as the thermal boundary condition makes it more difficult for our numerical schemes to converge on eigenvalues.

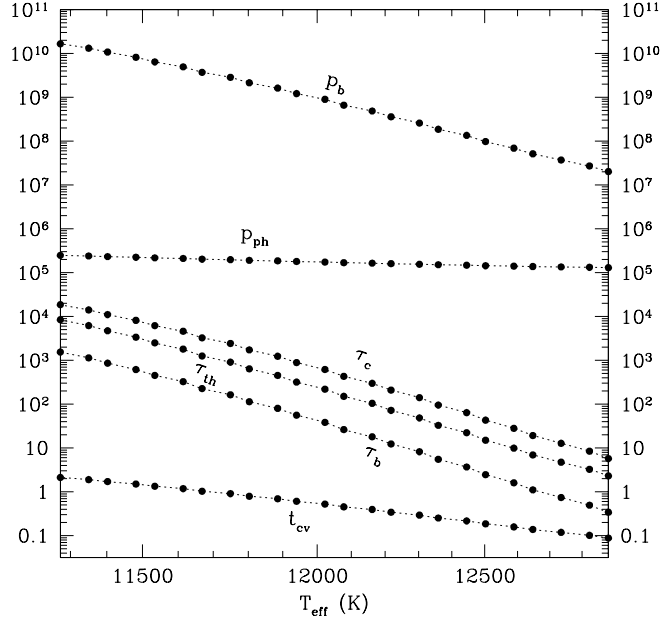


Fig. 1.— Convection zone characteristics for a sequence of hydrogen envelope models covering the temperature range where ZZ Ceti reside. Models have surface gravity, $g = 10^8 \text{ cm s}^{-2}$, and convection parameter, $f = 0.32$. Photospheric pressure (p_{ph}) and pressure at $z_b(p_b)$ are in units of dyne cm^{-2} . Time constants t_{cv} , τ_b , τ_{th} , and τ_c are in units of s. Both t_{cv} and τ_{th} are evaluated at z_b . Observationally detected g-modes have periods in the range $10^2 - 10^3$ s.

2.4. Envelope Models

Instead of using complete white dwarf models, we work with plane-parallel, hydrogen envelopes computed on fine grids. These are produced by integrating downward from the photosphere³ using the Lawrence Livermore equation of state and opacity tables (Rogers et al. 1996, Iglesias & Rogers 1996). Our envelopes have $g = 10^8 \text{ cm s}^{-2}$ and cover the range $11,000 \text{ K} \leq T_{\text{eff}} \leq 13,000 \text{ K}$.

We model convection by invoking the mixing length ansatz. This involves introducing a dimensionless parameter f such that⁴

$$\frac{ds}{d \ln p} = \frac{f}{(|\rho_s| \rho p)^{\frac{1}{3}}} \left(\frac{m_p F_{\text{cv}}}{k_B T} \right)^{\frac{2}{3}}. \quad (20)$$

The parameter f is of order unity and is related to the conventional mixing length ratio α by $f \sim \alpha^{-4/3}$. A smaller f signifies more efficient convection and yields a thicker convection zone. The radiative flux is

³The photosphere is taken to be where $p = 2g/(3\kappa)$.

⁴See equation (23) of Paper I.

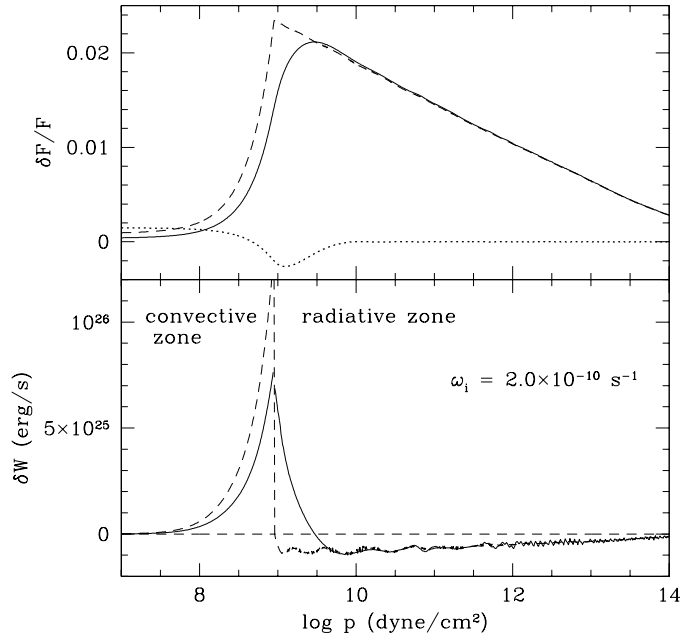


Fig. 2.— Comparisons of eigenfunctions calculated with and without the inclusion of radiative diffusion. The upper panel shows the fractional Lagrangian flux perturbation, $\delta F/F$, and the lower the differential work, defined by $W = \int \delta W d \log p$, both plotted against $\log p$. Results from quasiadiabatic calculations are depicted by dashed lines, whereas those from nonadiabatic calculations are given by solid lines for real parts and dotted lines for imaginary parts. We set the nonadiabatic $\delta F/F$ to have the same phase and amplitude as the quasiadiabatic one in the deep adiabatic interior. The stellar model has $T_{\text{eff}} = 12,000$ K, which with $g = 10^8 \text{ cm s}^{-2}$ and $f = 0.32$ yields $\tau_{\text{th}} = 200$ s at z_b . The mode shown here has $\ell = 1$ and $P = 430$ s. It is fairly adiabatic in the radiative region since $\omega \tau_{\text{th}} = 2.8$ at z_b . Nevertheless, radiative diffusion noticeably reduces convective driving and gives rise to a small region of radiative driving immediately below the convection zone.

related to the entropy gradient by

$$\frac{ds}{d \ln p} = \frac{3\kappa p F_{\text{rad}}}{16\sigma T^4 g} - \nabla_{ad}. \quad (21)$$

We determine $ds/d \ln p$, F_{cv} , and F_{rad} from equations (20) and (21) together with the relation $F = F_{\text{cv}} + F_{\text{rad}}$.

The grids of our model envelopes are chosen fine enough to resolve the steep entropy profiles in the superadiabatic layer. Figure 1 displays some characteristics of the surface convection zones in envelope models produced with $f = 0.32$. This value of f enables us to match our model to that of Bradley’s at $T_{\text{eff}} = 12,420$ K. Notice that the eddy turn-over time, t_{cv} , is of order a few seconds in even the coolest models of interest.

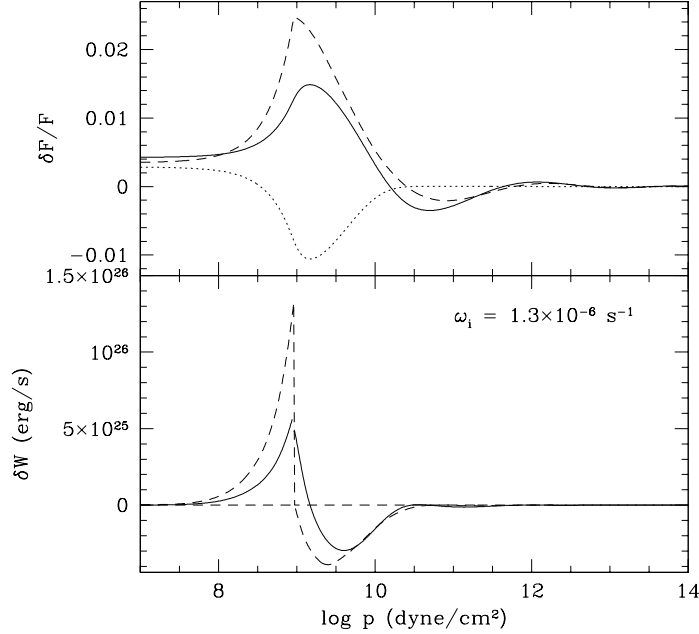


Fig. 3.— Similar to Figure 2, but for a mode with $\ell = 1$ and $P = 1,500$ s. Since $\omega\tau_{\text{th}} = 0.8$ at z_b , this mode is moderately nonadiabatic at the top of the radiative interior. The mode remains overstable when radiative diffusion is taken into account. However, the flux perturbation at the photosphere is modified in both amplitude and phase.

3. Where Nonadiabaticity Is Important

Nonadiabaticity is quantified by how much the presence of the entropy perturbation, δs , affects $\delta p/p$ and $\delta F/F$. Our analysis for the radiative interior leads to separate criteria for the evanescent region and the propagating cavity.

3.1. Nonadiabatic Effects in the Evanescent Region

The effect of δs on $\delta p/p$ is contained in equation (9). Noting that $\delta p/p$ varies on the scale $z_\omega > z$, we obtain

$$\frac{d}{d \ln p} \left(\frac{\delta p}{p} \right) \sim \frac{z}{z_\omega} \left(\frac{\delta p}{p} \right), \quad (22a)$$

$$\frac{dX}{d \ln p} \sim \frac{z}{z_\omega} \left(\frac{\delta p}{p} \right), \quad (22b)$$

$$\left(\frac{p}{\rho g} \right)^2 \left[k_h^2 \left(\frac{N^2}{\omega^2} - 1 \right) + \left(\frac{\omega}{c^2} \right)^2 \right] \left(\frac{\delta p}{p} \right) \sim \left(\frac{k_h z N}{\omega} \right)^2 \left(\frac{\delta p}{p} \right) \sim \frac{z}{z_\omega} \left(\frac{\delta p}{p} \right), \quad (22c)$$

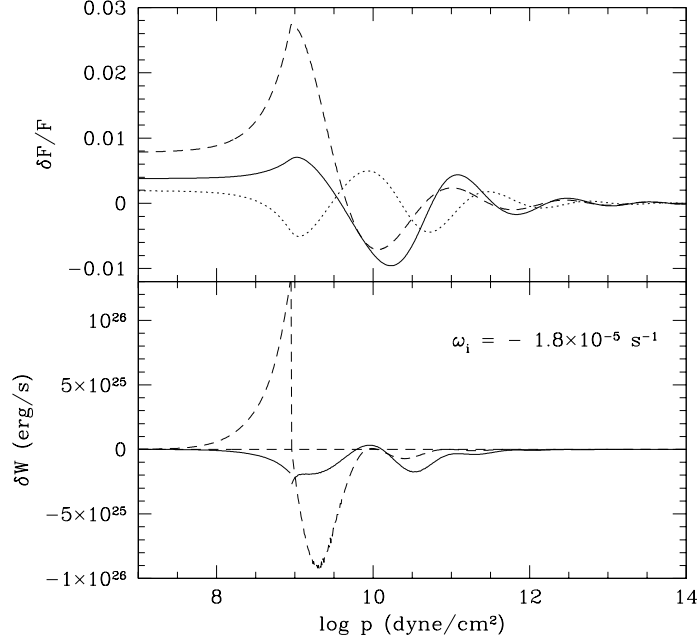


Fig. 4.— Similar to Figure 2, but for a mode with $\ell = 1$ and $P = 2,400$ s corresponding to $\omega_{\tau\text{th}} = 0.5$ at z_b . The nonadiabatic region extends down into the propagating cavity. There is a large phase difference between $\delta F/F$ and $\delta p/p$ at z_b which leads to convective damping. As a consequence, this mode is damped, although a quasiadiabatic calculation predicts overstability.

where $z \sim p/(g\rho)$ and $N^2 \sim g/z$. The nonadiabatic term is of order,

$$\frac{p}{\rho g} \frac{(gk_h)^2 - \omega^4}{g\omega^2} \rho_s \delta s \sim \frac{z}{z_\omega} \delta s. \quad (23)$$

So the nonadiabatic correction to $\delta p/p$ is of order δs .

To relate δs to $\delta p/p$, we turn to equations (10) and (11). With appropriate scalings they yield⁵

$$\delta s \sim \frac{1}{\omega\tau_{\text{th}}} \frac{d}{d \ln p} \left(\frac{\delta F}{F} \right) \sim \frac{1}{\omega\tau_{\text{th}}} \frac{\delta F}{F}, \quad (24a)$$

$$\frac{\delta F}{F} \sim \frac{\delta p}{p} + \delta s. \quad (24b)$$

Together, equations (23)-(24b) imply that the ratio of the nonadiabatic to adiabatic contributions to both $\delta p/p$ and $\delta F/F$ is of order $(\omega\tau_{\text{th}})^{-1}$, as is commonly cited in the literature.

⁵The coefficient connecting $\delta p/p$ to $\delta F/F$ in equation (11) varies on scale z , although weakly.

3.2. Nonadiabatic Effects in the G-Mode Cavity

Here, all perturbation quantities vary on a vertical scale k_z^{-1} , where $k_z z \geq 1$. Moreover, it follows from the local dispersion relation derived in Paper I that $k_z \sim (zz\omega)^{-1/2}$.

Scaling the adiabatic terms in equation (9) yields

$$\frac{d}{d \ln p} \left(\frac{\delta p}{p} \right) \sim (k_z z) \left(\frac{\delta p}{p} \right), \quad (25a)$$

$$\frac{dX}{d \ln p} \sim (k_z z)^2 \left(\frac{\delta p}{p} \right), \quad (25b)$$

$$\left(\frac{p}{\rho g} \right)^2 \left[k_h^2 \left(\frac{N^2}{\omega^2} - 1 \right) + \left(\frac{\omega}{c^2} \right)^2 \right] \left(\frac{\delta p}{p} \right) \sim \frac{z}{z_\omega} \left(\frac{\delta p}{p} \right) \sim (k_z z)^2 \left(\frac{\delta p}{p} \right). \quad (25c)$$

To order of magnitude, the nonadiabatic term is given by

$$\frac{p}{\rho g} \frac{(gk_h)^2 - \omega^4}{g\omega^2} \rho_s \delta s \sim \frac{z}{z_\omega} \delta s \sim (k_z z)^2 \delta s. \quad (26)$$

These equations imply that the nonadiabatic correction to $\delta p/p$ is of order δs .

We scale equations (10) and (11) to relate δs to $\delta p/p$;

$$\delta s \sim \frac{(k_z z)}{\omega \tau_{\text{th}}} \left(\frac{\delta F}{F} \right), \quad (27a)$$

$$\frac{\delta F}{F} \sim \frac{d}{d \ln p} \left(\frac{\delta p}{p} + \delta s \right) \sim (k_z z) \left(\frac{\delta p}{p} + \delta s \right). \quad (27b)$$

Combining equations (25c)-(27b), we determine that the ratio of nonadiabatic to adiabatic contributions to $\delta p/p$ and $\delta F/F$ is of order $(k_z z)^2 / \omega \tau_{\text{th}}$. This is not surprising; $\tau_{\text{th}} / (k_z z)^2$ is the timescale of thermal diffusion across distance k_z^{-1} . Nonadiabaticity is measured by the ratio of the mode period to this timescale.

4. Solution Of Eigenvalue Problem

We follow a two step procedure in solving the linear pulsation equations (8)-(11) for the four dependent variables subject to the five boundary conditions given by equations (15)-(19). The initial step consists of guessing a value for the complex eigenfrequency and then applying a relaxation method (cf. Press et al. 1992) to solve the differential equations subject to four out of the five boundary conditions.⁶ The step is complete when the dependent variables satisfy both the pulsation equations and the boundary conditions to 10^{-7} of a scaling factor provided by the corresponding adiabatic eigenfunction at individual points. Working in double precision, this is routinely achieved. The second step determines the eigenvalue by requiring the remaining boundary condition to be satisfied. Both minimization and root finding techniques work well. Normally we reserve equation (18) for our fifth boundary condition, but identical results are obtained when others are used instead.

⁶The trivial boundary condition given by equation (15) is always included as one of this foursome.

4.1. Eigenvalues for Stellar G-Modes

Nonadiabatic eigenvalues of our plane-parallel hydrogen envelopes are denoted by primes, $\omega' = \omega'_r + i\omega'_i$. To relate ω'_i to ω_i of a complete DA white dwarf model, we proceed as follows. We compute adiabatic modes for a corresponding complete model and identify those whose frequencies bracket ω'_r .⁷ We determine by interpolation the non-integer number n of nodes in $\delta p/p$ to assign to the adiabatic mode of the complete model whose frequency $\omega = \omega'_r$. Suppose that n' of these nodes lie above z_{deep} . Then

$$\omega_i \approx \frac{n'}{n} \omega'_i. \quad (28)$$

Validation of equation (28) is provided by equation (A7) in the appendix. Its physical justification is that whereas energy is dissipated near the surface, it is stored throughout the mode cavity.

Our procedure for converting ω'_i to ω_i requires nonadiabatic effects to be small well above z_{deep} , as is the case for all modes of interest to our investigation. However, it only applies to modes which have at least one node above z_{deep} . Thus it cannot handle the highest frequency g-modes. Values of ω_i for these are computed from the work integral.

Very low order modes ($n \leq 6$) are evanescent above z_{deep} . We therefore cannot enforce the boundary condition equation (18) on them to solve for the eigenvalues. We rely on work integral for stability analysis of these modes.

4.2. The Work Integral

Calculating the work integral provides an approximate method for evaluating the driving or damping rate of a mode. The work integral computes $\gamma = 2\omega_i$. This method is well defined and accurate when the quasiadiabatic approximation applies. Moreover, it reveals regions of driving and damping. Since overstable g-modes of ZZ Ceti have high quality factors, their linear pulsations are nearly periodic. The work integral may be calculated as follows (Unno et al. 1989):

$$\begin{aligned} \gamma &= \frac{\omega_r R^2}{2\pi} \oint dt \int_0^R dz \rho \frac{k_B}{m_p} \delta T \frac{d\delta s}{dt} \\ &= \frac{\omega_r R^2}{2} \int_0^R dz \nabla_{ad} \rho \frac{k_B}{m_p} T \left[\left(\frac{\delta p}{p} \right)_r \delta s_i - \left(\frac{\delta p}{p} \right)_i \delta s_r \right]. \end{aligned} \quad (29)$$

5. Numerical Results

5.1. Nonadiabatic Effects On Eigenfunctions

The effects of nonadiabaticity are illustrated by comparing nonadiabatic and adiabatic eigenfunctions for three $\ell = 1$ g-modes of the same stellar model. The model is characterized by $T_{\text{eff}} = 12,000$ K, $g = 10^8 \text{ cm s}^{-2}$, and $f = 0.32$, which together imply $\tau_{\text{th}} \approx 200$ s at $z = z_b$. The modes have periods of 430 s, 1,500 s, and 2,400 s. Quasiadiabatic calculations predict overstability for each of these modes.

⁷The adiabatic modes have the same ℓ as the mode of the plane-parallel envelope.

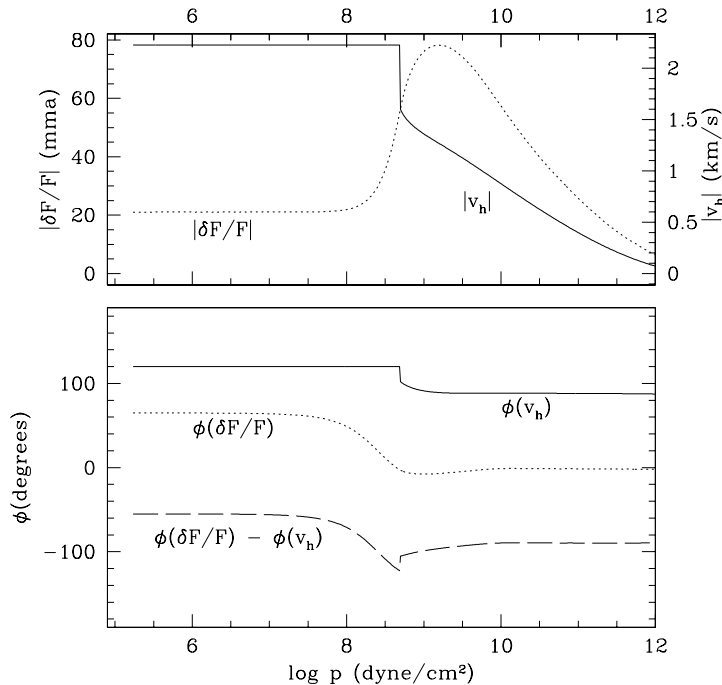


Fig. 5.— Amplitudes and phases of $\delta F/F$ and v_h as functions of $\log p$. The displayed mode has $\ell = 1$ and $P = 800$ s corresponding to $\omega\tau_{\text{th}} = 0.8$ at $z = z_b$ in a stellar model with $T_{\text{eff}} = 12,160$ K, $g = 10^8$ cm s⁻², and $f = 0.32$. The amplitude, $|X|$, and phase, ϕ , of a perturbation X are defined as $X = |X| \cos(\omega t - \phi)$. In the adiabatic interior, the flux perturbation leads the velocity perturbation by 90°.

Radiative diffusion acts to soften sharp temperature gradient perturbations. Its importance increases with mode period. These characteristics are illustrated in Figures 2-4.⁸ The 430 s mode, with $\omega\tau_{\text{th}} = 2.8$ at $z = z_b$, is quite adiabatic in the radiative interior. Radiative diffusion is more pronounced in the evanescent region of the 1,500 s mode, which has $\omega\tau_{\text{th}} = 0.8$ at $z = z_b$. The nonadiabatic eigenfunction of the 2,400 s mode, for which $\omega\tau_{\text{th}} = 0.5$ at $z = z_b$, deviates significantly from its adiabatic counterpart in both the evanescent and propagating regions. The phase shift between $\delta F/F$ and $\delta p/p$ at z_b is so large that the convection zone contributes to mode damping. This mode is stable.

The recent detection of velocity signals associated with g-modes by van Kerkwijk et al. (1998) is an important advance in the study of ZZ Ceti. What is being detected are horizontal velocities near the stellar limb. Phase differences and amplitude ratios of flux and velocity variations due to individual modes offer unique clues about both the star and the modes. Nonadiabatic calculations, such as that depicted in Figure 5, provide a theoretical basis for interpreting these observable quantities. Deep inside the radiative interior, the maximum flux perturbation precedes the maximum horizontal velocity by a quarter of a period, and the flux to velocity amplitude ratio is determined by the quasiadiabatic approximation. These

⁸We normalize $\delta p/p$ at $z = z_{\text{deep}}$ by setting it equal to its adiabatic counterpart. Thus the imaginary component of $\delta F/F$ is due to nonadiabaticity.

relations are modified in the upper envelope by the convective transport of heat and momentum and by radiative diffusion. Convection delays and diminishes the flux variation (see Paper I). It also flattens the horizontal velocity profile above z_b and forces it to jump at z_b (see Paper II). Radiative diffusion smears flux perturbations below the convection zone. In the example illustrated in Figure 5, a photospheric flux variation of 20 mma⁹ corresponds to a horizontal velocity of $v_h = 2.3 \text{ km s}^{-1}$. Nonadiabaticity, mostly in the convection zone, reduces the phase lag between velocity maximum and light maximum from the quasiadiabatic value of 90° to 55° at the photosphere. Employing the conventions in van Kerkwijk et al. (1998), this mode would exhibit $R_v = |v_h|/(\omega|\delta F/F|) = 16$, and $\Delta\Phi_v = \Phi(\delta F/F) - \Phi(v_h) = -55^\circ$. This is consistent with the 818 s mode which they observed to have $R_v = 11 \pm 4$ and $\Delta\Phi_v = -44^\circ \pm 19^\circ$.¹⁰

5.2. Nonadiabatic Effects On Driving and Damping Rates

Where applicable, direct calculations of ω_i yield results consistent with those based on the work integral. This provides a measure of confidence in both. Modest discrepancies are found for some marginally overstable modes. The eigenvalue calculations are more reliable, as work integrals suffer from inaccuracies due to cancellation between comparable magnitudes of driving and damping. Values of ω_i for individual g-modes evolve with decreasing T_{eff} . Effects of nonadiabaticity on driving and damping rates of g-modes are presented in Figures 6-7. General trends are described below.

Upper lids of cavities of short period modes (e.g., the 430 s mode) lie far beneath the bottom of the convection zone in even in the coolest variables. Their driving/damping rates are largely immune to both nonadiabatic effects and the depth of the convection zone, and hardly vary across the instability strip. The quasiadiabatic estimate, $\omega_i \sim 1/(n\tau_\omega)$, pertains to these modes (see Paper I).

Longer period modes (e.g., the 1,000 s mode) become overstable at lower T_{eff} . Values of their $|\omega_i|$ exhibit a steady decline with decreasing T_{eff} . This is a consequence of the increase in mode inertia with decreasing T_{eff} . As the convection zone deepens, it depresses the upper lid of a mode's cavity. This decreases the relative size of the perturbation amplitude near the surface, where nonadiabaticity is greatest, with respect to that in the interior, where most of the mode energy is stored.

Modes with even longer periods (e.g., the 2,000 s mode) are weakly overstable in cooler and narrower temperature ranges. Nonadiabatic effects tend to stabilize these modes. In the limit of strong dissipation, $\omega_i/\omega_r \approx -\ln \mathcal{R}^{-1}/(2\pi n)$, where \mathcal{R} is the reflection coefficient at the cavity lid. We derive this relation using a toy model in the appendix. Magnitudes of nonadiabatic damping rates are an important input to calculations of parametric instability, an amplitude limiting mechanism for overstable modes that is explored in the next paper of this series.

6. Maximum Periods of Overstable Modes

⁹Milli-magnitude-amplitude is the commonly adopted unit for measuring flux perturbations. An 1 mma variation means $\delta F/F = 10^{-3}$.

¹⁰Effects of limb-darkening, disc averaging, and bolometric correction introduce a factor close to unity.

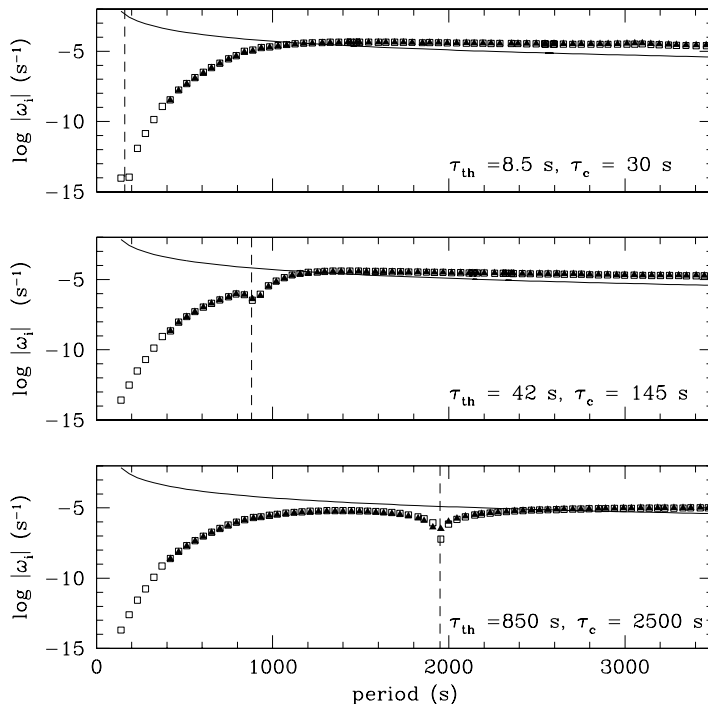


Fig. 6.— Driving and damping rates for $\ell = 1$ modes plotted against mode periods. Top to bottom, the panels pertain to stellar models computed with $g = 10^8 \text{ cm s}^{-1}$ and $f = 0.32$ for $T_{\text{eff}} = 12,600 \text{ K}$, $12,300 \text{ K}$, and $11,750 \text{ K}$. Values of $|\omega_i|$ obtained from the nonadiabatic code are denoted by solid triangles. Those calculated from work integrals using nonadiabatic eigenfunctions are shown by open squares. For very short periods, $P < 400 \text{ s}$, our shallow envelopes force us to rely entirely on the work integral. The dashed vertical line marks the boundary between shorter period overstable modes and longer period damped ones. The solid line displays the analytic estimate, $\omega_i = -\omega_r \ln \mathcal{R}^{-1}/(2\pi n)$, for the damping rate of modes which suffer strong dissipation. We set $\mathcal{R} = 1/e$ here, although in reality it decreases with increasing mode period and effective temperature.

6.1. Limitations of the Overstability Criterion $\omega\tau_c > 1$

The derivation of the overstability criterion $\omega\tau_c > 1$ depends on the quasiadiabatic approximation and the condition that $z_\omega \gg z_b$ (Brickhill 1991, Paper I). Since $\tau_c \approx 4\tau_{\text{th}}$ at z_b , the quasiadiabatic approximation is suspect for modes with $\omega\tau_c \approx 1$. The upper and lower panels of Figure 7 display the boundary between overstable and damped modes as determined by quasiadiabatic and nonadiabatic calculations. Both show that the boundary value of $\omega\tau_c$ is close to unity for hot ZZ Ceti stars but rises as stars cool. Inaccuracy of the quasiadiabatic approximation does not dramatically modify the overstability criterion, but the violation of the condition $z_\omega \gg z_b$ does. The latter occurs because z_b increases with decreasing T_{eff} and z_ω decreases with decreasing ω . Modes with $z_\omega \lesssim z_b$ propagate just below z_b . Their short WKB wavelengths enhance radiative damping above the estimate given by equation (54) in Paper I on which the derivation of the overstability criterion $\omega\tau_c > 1$ rests.

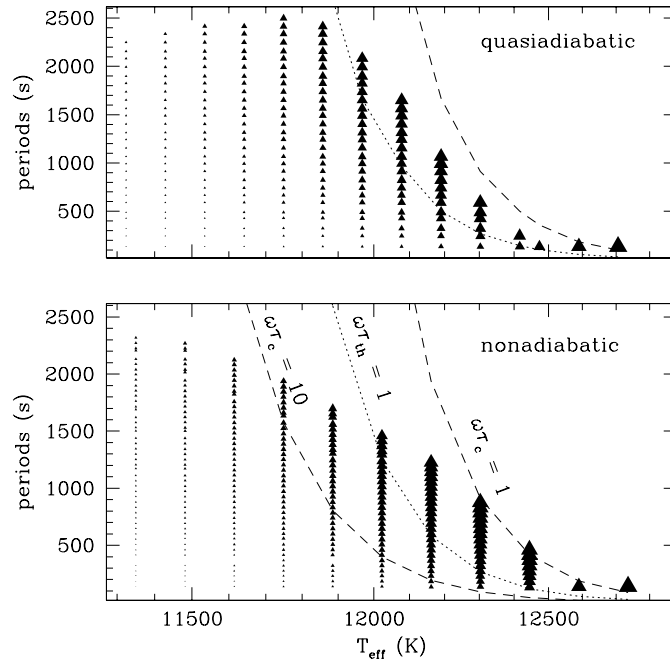


Fig. 7.— Panoply of overstable $\ell = 1$ modes according to quasiadiabatic (upper panel) and fully nonadiabatic (lower panel) calculations in white dwarf models produced with $g = 10^8 \text{ cm s}^{-1}$ and $f = 0.32$ for a range of T_{eff} which covers the ZZ Ceti instability strip. Each overstable mode is marked by a solid triangle whose size is proportional to the diminution factor of the flux perturbation in the convection zone, $[1 + (\omega\tau_c)^2]^{-1/2}$ (see Paper I). Dashed lines denote the loci of constant values of $\omega\tau_c$. The dotted line corresponds to $\omega\tau_{\text{th}} = 1$ with τ_{th} evaluated at $z = z_b$.

6.2. Comparison with Observations

Both our quasiadiabatic and nonadiabatic calculations consistently predict maximum periods for overstable modes that are about a factor two longer than those observed (cf. Fig. 8). We have not been able to resolve this discrepancy. Several possible explanations which we have considered are described in what follows.

6.2.1. Effects of Turbulent Damping

Both Brickhill (1990) and Paper II stress that linear damping due to turbulent viscosity, although negligible inside the convection zone for all modes, may be significant in the region of convective overshoot for long period modes. We incorporate this effect into our analysis, while recognizing that it cannot be quantified precisely.

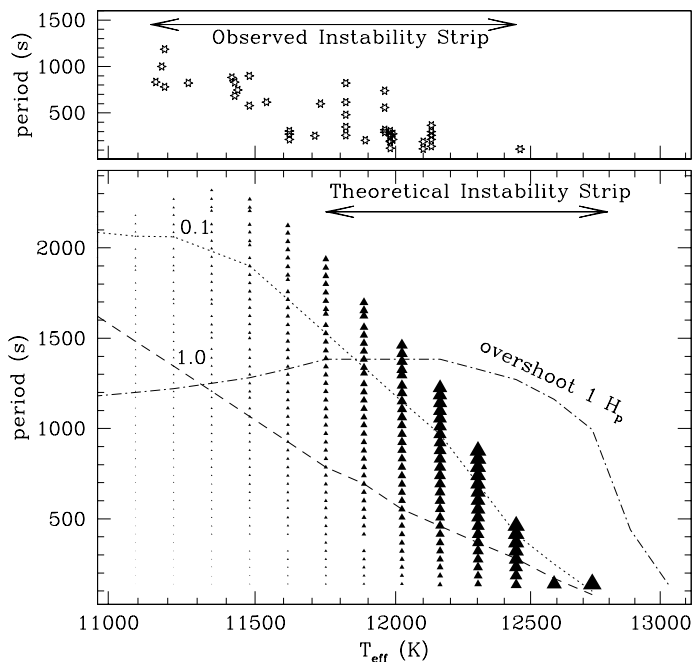


Fig. 8.— Observational and theoretical instability strips for DA white dwarfs. The upper panel displays each of the known ZZ Ceti according to the dominant period in its pulsation spectrum (Bradley 1996), and its inferred effective temperature (Bergeron et al. 1995). The lower panel repeats the material shown in the lower panel of Figure 7. The dotted and dashed lines illustrate the maximum period for overstable modes under the stabilizing effect of turbulent damping in the region of convective overshoot for values of the parameter λ/z_b equal to 0.1 and 1.0, respectively. The dotted-dashed line shows the envelope of overstable modes for models which incorporate one pressure scale height of convective overshoot. When comparing observational and theoretical instability strips, one should bear in mind that both depend upon the assumed mixing-length.

The rate of turbulent damping in the overshoot region is expressed as (eq. [36] in Paper II),

$$\gamma_{\text{vis-os}} \approx \frac{-\pi R^2 \rho_b \omega^3 \lambda |\Delta \xi_h|^2}{4}, \quad (30)$$

where $|\Delta \xi_h|$ is the normalized jump in the horizontal displacement across the convective overshoot region within which the turbulent viscosity decays on length scale λ . To cover our ignorance, we present results for λ/z_b of 0.1 and 1.0. Figure 8 demonstrates that with the larger value, the longest period overstable mode at a given T_{eff} is compatible with the observed upper limit of $P = 1,200$ s. However, it seems unlikely that $\lambda/z_b \approx 1$. The overshoot region probably extends less than a pressure scale height below z_b , while $H_p \approx 0.4z_b$, and λ must be several times smaller than H_p .

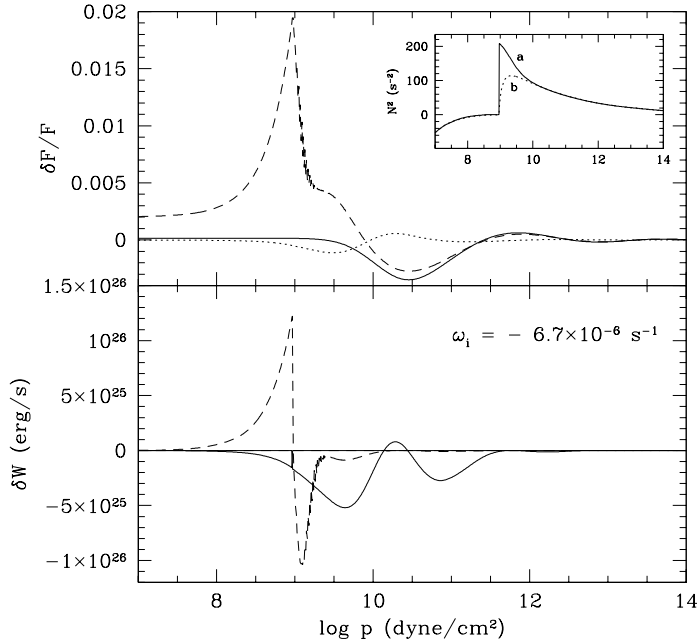


Fig. 9.— Effects of convective overshoot on g-mode structure and stability. The stellar model lies at $T_{\text{eff}} = 12,250$ K with one pressure scale height of overshoot below the convection zone. We use the same mode as in Figure 3, and the stellar model there has a convection zone as deep as the bottom of the overshoot region in this model. The small inset in the top panel shows the Brunt-Väisälä frequencies for the former in dashed line (labelled with 'b') and the latter in solid line (labelled with 'a'). The top and bottom panels display similar materials as in Figure 3, except that the nonadiabatic work integral is multiplied by a factor of 20 to aid display. Both quasiadiabatic and nonadiabatic calculations predict stability for this mode.

6.2.2. Effects of Convective Overshoot

We modify our envelope models to simulate convective overshoot by adding an isentropic layer below the base of the convection zone. Within this layer the radiative flux exceeds the total flux and turbulence transports energy downward. The top of the radiative interior immediately below the overshoot layer differs from that below a convective layer of similar depth. The temperature gradient is shallower and the Brunt-Väisälä frequency has a finite positive value. These differences enhance the effects of radiative diffusion and modify the relations between horizontal velocity and light perturbations at the photosphere.

Figure 9 provides such an example. Our nonadiabatic calculations indicate that one pressure scale height of overshoot suffices to stabilize all modes with $P > 1,400$ s (see Fig. 8). Moreover, by effectively deepening the convection zone, it shifts the instability strip to higher T_{eff} .

6.2.3. Sensitivity to Surface Gravity

Our nonadiabatic calculations indicate that, at fixed T_{eff} , the longest period for an overstable mode scales approximately as $g^{-1/3}$. Thus maximum periods of overstable modes around 1,200 s would require $g \approx 5.0 \times 10^8 \text{ cm s}^{-2}$, which is well outside observational constraints.¹¹

6.2.4. Other Observational and Theoretical Considerations

Hansen et al. (1985) show that damping due to upward propagation of a gravity wave above the photosphere is unimportant for modes having frequencies exhibited ZZ Ceti. We concur with this conclusion.

Detection of lower frequency modes requires longer observational data streams. Noise due to variations of atmospheric transparency increases at lower frequencies (see Fig. 4 of Winget 1991). These may result in an observational bias against the detection of low frequency modes.

Evidence that photometric amplitudes of modes decline for $P \gtrsim 1,000$ s, suggests that the observational cutoff at $P \approx 1,200$ s is genuine (see Fig. 5 in Clemens 1995). Taken literally, it also hints that the cutoff is the result of a nonlinear mechanism which saturates pulsation amplitudes.

7. Summary

There is little doubt that convective driving, as originally proposed by Brickhill (1991), is responsible for the linear overstability of g-modes in DA white dwarfs. It is physically self-consistent, and convincingly rationalizes observational facts. It accounts for the general location of the instability strip, although a precise specification depends upon the modeling of convection (e.g., the mixing-length parameter). Convective driving also explains why longer period modes become overstable as a star cools (see Fig. 8).

Although we agree with Brickhill that $\omega\tau_c > 1$ is a necessary condition for mode overstability, we find that it is not a sufficient condition for modes whose periods exceed 1,000 s. This stems from enhanced radiative damping of modes whose upper cavity lids approach z_b , as is apparent from both quasiadiabatic and nonadiabatic calculations (see Fig. 7). Our nonadiabatic calculations yield a maximum period of about 2,300 s for overstable modes. This clashes with the maximum period of 1,200 s for observationally detected modes.

We also agree with Brickhill's deduction (1990) that turbulent convection forces the horizontal velocity to be nearly independent of depth within the convective envelope. Consequently, mode damping due to turbulent dissipation within the convection zone is reduced to a negligible level. However, suppression of the horizontal shear in the convective envelope results in a shear layer at the top of the radiative interior. When convective overshoot is accounted for, this provides linear turbulent damping. Figure 8 suggests that turbulent dissipation might depress the maximum period of observable modes to some degree. Convective overshoot also alters the thermal structure of the upper radiative layer. A rough treatment of this effect with one scale height of overshoot predicts a maximum period of 1,400 s for overstable modes. Nonlinear

¹¹Applying a theoretical mass-radius relation (Hamada & Salpeter 1961) for white dwarfs, this corresponds to a stellar mass about $1.2M_{\odot}$.

interactions which limit the amplitudes of overstable modes may also play a part in determining the maximum period.

In conclusion, the blue edge of the theoretical instability strip seems to be set by the condition that $\omega\tau_c \approx 1$ for the lowest order $\ell = 1$ mode. But the location of the red edge is more nebulous, and may result from a combination of decreased photometric visibility, convective overshoot, and nonlinear effects. Additional detections of velocity variations associated with g-modes could provide important clues. Convective driving makes the testable prediction that velocity variations become relatively more observable than photometric variations toward the red edge of the instability strip.

REFERENCES

- Bergeron, P., Wesemael, F., Lamontagne, R., Fontaine, G., Saffer, R. A., & Allard, N. F. 1995, *ApJ*, 449, 258
- Bradley, P. A. 1995, *Baltic Astronomy*, 4, 536
- Bradley, P. A. 1996, *ApJ*, 468, 350
- Brickhill, A. J. 1990, *MNRAS*, 246, 510
- Brickhill, A. J. 1991, *MNRAS*, 251, 673
- Clemens, J. C. 1995, *Baltic Astronomy*, 4, 142
- Gautschy, A., Ludwig, H. G., & Freytag, B. 1996, *A&A*, 311, 493
- Goldreich, P. & Wu, Y. 1998, *ApJ*, accepted for publication, (Paper I)
- Goldreich, P. & Wu, Y. 1998, *ApJ*, submitted, (Paper II)
- Hamada, T. & Salpeter, E. E. 1961, *ApJ*, 134, 683
- Hansen, C. J., Winget, D. E. & Kawaler, S. D. 1985, *ApJ*, 297, 544
- Iglesias, C.A., & Rogers, F. J. 1996, *ApJ*, 464, 943
- van Kerkwijk, M. H., Clemens, J. C., Wu, Y. 1998, submitted to *MNRAS*
- Press, W. H., Teukolsky, S. A., Vetterling, W. T., & Flannery, B. P. 1992, *Numerical Recipes in Fortran*, (Cambridge University Press), 403, 753,
- Rogers, F. J., Swenson, F. J. & Iglesias, C. A. 1996, *ApJ*, 456, 902
- Winget, D. E., Nather, R. E., Clemens, J. C. et al., 1991, *ApJ*, 378, 326
- Unno, W., Osaki, Y., & Ando, H. 1989, *Nonradial Oscillations of Stars*, (University of Tokyo Press), 238

A. A Toy Model For Nonadiabatic Modes

We describe a simple toy model for nonadiabatic modes. It is particularly useful for interpreting damping rates in the limit of strong dissipation.

Consider waves which satisfy the one-dimensional, homogeneous, acoustic wave equation

$$\frac{\partial^2 \xi}{\partial t^2} = u^2 \frac{\partial^2 \xi}{\partial z^2}, \quad (\text{A1})$$

in the interval $0 \leq z \leq L$. Here ξ is the Lagrangian displacement and u is the constant propagation speed. The dispersion relation connecting frequency, ω , and wave vector, k , reads $\omega^2 = k^2 u^2$. We take the lower boundary to be a rigid, perfectly reflecting wall, so

$$\xi = 0 \quad \text{at} \quad z = L. \quad (\text{A2})$$

Dissipation is introduced by means of a partially reflective upper boundary, where \mathcal{R} denotes the reflection coefficient of the incident wave. This is expressed through the boundary condition

$$\left(\frac{\partial}{\partial t} - u \frac{\partial}{\partial z} \right) \xi = -\mathcal{R} \left(\frac{\partial}{\partial t} + u \frac{\partial}{\partial z} \right) \xi \quad \text{at} \quad z = 0. \quad (\text{A3})$$

Note that in the limit $\mathcal{R} \rightarrow 1$, the upper boundary becomes a perfectly reflecting wall.

Eigen-solutions of equation (A1) are composed of oppositely directed waves;

$$\xi = A e^{-i\omega t - ikz} + B e^{-i\omega t + ikz}. \quad (\text{A4})$$

Application of the boundary conditions given by equations (A2) and (A3) yields

$$B = -\mathcal{R}A, \quad (\text{A5})$$

and

$$kL = n\pi - \frac{i}{2} \ln \mathcal{R}^{-1}, \quad (\text{A6})$$

where n is the number of half wavelengths between the walls. Then the dispersion relation implies

$$\omega_i = \frac{k_i}{k_r} \omega_r = -\frac{\omega_r}{2\pi n} \ln \mathcal{R}^{-1}, \quad (\text{A7})$$

where n is an integer.

Equation (A7) is the key result of our toy model. It demonstrates that ω_i grows logarithmically with \mathcal{R}^{-1} , and provides an order-of-magnitude estimate for the damping rate of strongly nonadiabatic stellar modes. Radiative diffusion substantially suppresses the effective reflection coefficients of modes having $\omega\tau_\omega \leq 1$. In hot DA stars, this applies to modes with periods in excess of 1,000 s (cf. Fig. 6). Finally, equation (A7) justifies the procedure we apply in §4.1 to translate ω'_i , the damping rate for a mode of an envelope model, to ω_i , the damping rate for a mode of a complete stellar model.